



1 **Supernova effects on middle and upper atmospheric nitric oxide and** 2 **stratospheric ozone**

3 **¹David E. Siskind, ²McArthur Jones Jr., ^{2,3}Jeffrey W. Reep**

4 ¹Computational Physics Inc., Springfield, VA, USA

5 ²Space Science Division, Naval Research Laboratory, Washington, DC, USA

6 ³ now at Institute for Astronomy, University of Hawaii at Mānoa, Pukalani, HI, USA

7
8 Corresponding authors:

9 David Siskind (dsiskind@cpi.com)

10 McArthur Jones Jr. (mcarthur.jones16.civ@us.navy.mil)

11

12 **Abstract**

13 We provide a quantitative test of the recent suggestion (Brunton et al., 2023) that supernovae
14 could significantly disrupt planetary ozone layers through a multi-month flux of soft X-rays that
15 produce ozone-destroying odd nitrogen (e.g. NO and NO₂). Since soft X-rays do not directly
16 penetrate down to the ozone layer, this effect would be indirect and require downward transport
17 of NO_x from the mesosphere. Mirroring previous studies of the indirect effects of energetic
18 particle precipitation (EPP-IE), we call this the X-ray Indirect Effect (Xray-IE). We use the
19 NCAR Thermosphere-Ionosphere-Mesosphere-Electrodynamics General Circulation Model
20 (TIME-GCM) to simulate the production of NO and its transport into the stratosphere. We model
21 the soft X-ray flux as if it were a multi-month long solar flare and use our previously developed
22 solar flare model to simulate the soft X-ray enhancement. Our results yield significant
23 enhancement in stratospheric odd nitrogen, most dramatically in the Southern Hemisphere. The
24 most global effects are seen in the upper stratosphere at pressure surfaces between 1-3 hPa
25 (about 42-48 km) consistent with previous observations of the EPP-IE. We then use a detailed
26 stratospheric photochemistry model to quantify the effects of this NO_x enhancement on ozone.
27 Widespread ozone reductions of 8-15% are indicated; however, because these are limited to the
28 upper edges of the ozone layer, the effects on the ozone column are limited to 1-2%. We thus
29 conclude that the effects of a multi-month X-ray event on biologically damaging UV radiation at
30 the surface is also likely to be small.

31 **1. Introduction**

32 As discussed by Airapetian et al., (2019) and summarized by Garcia-Sage (2023), the explosion
33 of new discoveries of exoplanets and the search for life in the universe as led to increased recent
34 interest in how space weather can influence the climate and habitability of the earth and possible
35 life-bearing exoplanets. As the above articles discuss (see also Kahler and Ling, 2023), these
36 extreme space weather events can include solar/stellar flares, coronal mass ejections, solar/stellar
37 energetic particles (SEPs) and/or cosmic rays. There is, however, a parallel line of inquiry that
38 has long considered the effects of supernovae on planetary biospheres (Gehrels., et al., 2003). As
39 we will discuss, there is significant conceptual overlap in the specific mechanisms, which is a
40 motivation for our present study.



41 Recently Brunton et al (2023) have proposed a new mechanism by which supernovae could
42 threaten the existence of planetary biospheres. The classical mechanisms have traditionally
43 invoked ozone depletion either due to gamma ray emission which would occur promptly (within
44 100 days) with the event, or from cosmic ray fluxes which could be emitted over a period on the
45 order of 10-100 years (Gehrels, et al., 2003). Brunton et al., (2023) suggest a third mechanism
46 from enhanced X ray emissions that might result from interactions between the supernova blast
47 wave and the local interstellar medium. They present observed light curves showing X-ray
48 emissions occurring over periods ranging from 6 months to several years after the initial
49 eruption. They suggest that these emissions might represent a heretofore unexplored mechanism
50 for planetary ozone destruction.

51 An important consideration for understanding the effect of enhanced X-rays on the ozone layer,
52 which Brunton et al (2023) discuss, is the fact that X-rays with energies less than 10-20 keV are
53 absorbed in the mesosphere, above the ozone layer. While Brunton et al., recognize that there
54 may be X-ray emission from a supernova with greater energies, much of their data is limited to
55 these softer X-rays. As a result, they suggest that the effect of X-rays would be more indirect and
56 they quote some aeronomic studies (Solomon et al., 1982; Randall et al., 2006) of how
57 perturbations to nitric oxide in the mesosphere and lower thermosphere could be transported
58 down to the middle atmosphere where they would catalytically lead to ozone loss.
59 Conventionally this coupling mechanism is due the production of nitric oxide (NO) in the auroral
60 zones near 100 km altitude by energetic electron impact on N₂ followed by descent through the
61 mesosphere into the stratosphere under the cover of polar night which limits the dissociation of
62 the enhanced NO by UV sunlight. Randall et al., (2007) labeled this as the Energetic Particle
63 Precipitation Indirect Effect (EPP-IE). Here, motivated by Brunton et al.'s hypothesis, we
64 consider an analogous indirect effect on stratospheric odd nitrogen and ozone from continual soft
65 X-ray influx, which we dub the "X-ray IE".

66 Brunton et al. (2023) provide estimates for the total amount of X-ray energy that might threaten
67 planetary ozone layers and compared them to the integrated energy emitted by a multi-year solar
68 flare. Specifically, they argue that a so-called Carrington flare (X45, i.e. $4.5 \times 10^{-3} \text{ W m}^{-2}$), near
69 the upper limit of flare energy release by the Sun (see e.g. Cliver et al 2022), would have to
70 persist for 2.8 years to provide the requisite energy. Using this analogy, we will use an existing
71 solar flare model (Siskind et al., 2022) and consider the consequences of previously considered
72 solar flares extending for over a year. We will show how the X-ray IE can lead to a significant
73 influx of nitric oxide entering the stratosphere and quantitatively model to what extent this influx
74 could reduce ozone abundances. Ultimately, we conclude that due to the specifics of how NO is
75 transported in the middle atmosphere, while significant effects are probable, the global
76 destruction of the Earth's ozone layer is less likely.

77 The general outline of the paper is as follows. In Section 2, we introduce the solar flares that
78 form the basis of our study, look at the initial response of lower thermospheric NO and compare
79 our calculations with previously published observations of the nitric oxide response to solar flare.
80 In Section 3 we document the descent of this flare-produced NO down through the mesosphere
81 using a three-dimensional model of chemistry and transport of the middle and upper atmosphere



82 (the NCAR Thermosphere Ionosphere Mesosphere Electrodynamics General Circulation Model
83 (TIME-GCM)). To validate the X-ray IE we will put it into context of our calculated EPP-IE
84 which can be compared with the extensive literature on that topic. Finally, in Section 4, we
85 perform photochemical modeling of the sensitivity of stratospheric ozone to the various
86 enhancements in middle atmospheric nitric oxide suggested by the TIME-GCM. One limitation
87 that we will discuss is that the 30 km bottom boundary of the TIME-GCM is right at the peak of
88 the ozone layer. Thus our photochemical simulations are required to be able to extrapolate down
89 to encompass the entire ozone column.

90

91 **2. Solar Flare and thermospheric NO modeling**

92 2.1. Solar Flare modeling

93 Our approach follows the suggestion of Brunton et al. (2023), namely, to model the multi-month
94 soft X-ray flux as if it were a solar flare that lasted for months rather than the 30-60 minutes
95 which is typical (cf. Rodgers et al., 2010; Table 3; also Reep et al., 2023). The advantage of this
96 approach is that it allows us to utilize existing flare spectra (Siskind et al., 2022). These spectra
97 were developed with the NRLFLARE model, a physical model of solar flare irradiance, which
98 uses a series of flaring loop simulations to reconstruct the soft X-ray light curves of both
99 GOES/XRS channels, and from those loop simulations, synthesizes full spectra from
100 approximately 0.01 to 200 nm (Reep et al 2020; Reep et al 2022). The ratio of the two
101 GOES/XRS channels is commonly used as a proxy for temperature, which the model uses to
102 derive heating rates to drive those simulations (see e.g. Garcia 1994). The loop simulations are
103 run with the open-source radiative hydrodynamics code HYDRAD (Bradshaw & Cargill 2013;
104 Reep et al 2019, <https://github.com/rice-solar-physics/HYDRAD>), which solves the Navier-
105 Stokes equations for plasma constrained to travel along a magnetic flux tube. The full model and
106 spectral synthesis are described in detail in Reep et al 2022.

107 NRLFLARE was designed to reproduce X-ray spectra from solar flares, so it is important to
108 discuss the differences and similarities to supernova X-ray spectra. In both cases, the spectra in
109 soft X-rays (around 1 to 20 keV or so) are dominated by optically thin thermal bremsstrahlung
110 emission with a power law shape, with notable line emissions from hot ions such as Fe XXV (a
111 prominent line at 6.7 keV appears in spectra of both). There are two important differences.
112 First, the elemental abundances are not the same, which will cause the relative strength of the
113 emission (particularly line emission) to differ. Second, solar flares are expected to be in
114 collisional equilibrium, while supernova remnants have low enough densities that the collisional
115 timescale is long, so they are typically not in equilibrium. See the reviews by Vink (2012) for X-
116 ray emissions in supernovae and Fletcher et al. (2011) for solar flares (Sections 6 of both
117 reviews). For our purposes, the exact spectral shape is less important than the total energy input
118 driving the atmospheric response.

119 One of the main subjects of the Siskind et al., (2022) paper was the September 10, 2017 X8.3
120 flare and a spectrum at flare peak was presented in that paper. We will use that as our primary
121 case. Table 1 summarizes key aspects of that flare that are relevant for this paper. First, it is



122 important to note that in 2020, NOAA removed a 0.7 recalibration that had historically been
123 applied to GOES 13-15 data (cf.
124 https://ngdc.noaa.gov/stp/satellite/goes/doc/GOES_XRS_readme.pdf; also Reep et al., 2022)

125 Thus, the true X-ray irradiance for older flares is 1/0.7 brighter. This means that the 2017 flare,
126 originally labeled as 8.3 in Siskind et al. 2022 and earlier works (Qian et al., 2019; Redman et
127 al., 2018) should be re-classified as X11.8. Table 1 shows the calculated peak energy by the
128 NRLFLARE model as being about 12% greater than observed by GOES, thus effectively making
129 this flare an X13.3 event. We will thus use the label “X13” to describe this event as we discuss
130 our atmospheric simulations.

131 **Table 1**

Event	NOAA class	Calculated 0.1-0.8 X- class with NRLFLARE	Calculated energy flux, 0.1-1.0 nm (W/m ²)	Calculated energy flux, 1-2 nm (W/m ²)	Integrated energy ≥ 1 keV after 1 year (kJ/m ²)
Sept 10, 2017	11.8	13.3	1.55e-3	.0017	64.4
Oct 28, 2003	X25	X27	.004	.007	171.4

132

133 Table 1 also shows the integrated energy in several energy bins. The division into 0.1-1.0 nm and
134 1-2 nm bins is to compare with the calculations of Rodgers et al., (2010), discussed below. The
135 final column extrapolates our flare duration to a year. In particular, it shows that if we assumed
136 the X13 flare persisted for an entire year, it would deliver 64.4 kJ/m² to the atmosphere. This is
137 less than the 400 kJ/m² that Brunton et al., (2023) use as a critical threshold for ecologically
138 destructive X-ray energy input. We will therefore also consider the energy input from a spectrum
139 calculated for the October 28, 2003, the so-called Halloween event. The effects of this flare on
140 thermospheric nitric oxide were first discussed by Rodgers et al., 2010 and we will compare our
141 calculations to theirs. Again, due to the NOAA recalibration, this flare, which was originally
142 classified as X18, should really be classified as X25. As seen in Table 1, our calculated energy at
143 flare peak was about 8% higher than measured by GOES and thus we label this as an X27. If this
144 flare were to persist at peak level for a year, Table 1 indicates it would deliver about 171 kJ/m² to
145 the atmosphere. As shown by Brunton et al. (2023, their Figure 3), it is not uncommon for
146 supernova X-ray events to persist for over a year. Table 1 shows that if our calculated X27 event
147 were to last about 2.3 years it would deliver about 400 kJ/m² which is the energy input
148 postulated by Brunton et al. (2023) as being biospherically destructive. Unfortunately, the
149 problem with the X27 simulation is that when this spectrum was input continuously into the
150 atmospheric model (TIME-GCM, discussed below), the model crashed after 8 days of the
151 simulation. Thus, in our discussion of ozone chemistry effects, we will discuss extrapolations
152 based upon comparisons of the nitric oxide response from the first 8 days of each simulation.

153 Figure 1 compares the spectra from our X13 and X27 calculations at their respective peak
154 minutes. The figure shows the calculated spectrum at the native spectral resolution of



155 NRLFLARE (0.5 \AA) and then integrated in 1 nm bins so that it can be compared to that derived
156 by Rodgers et al (2010, see their Figure 3). Like Rodgers et al. (2010) our spectrum shows a
157 significant increase in the flare spectrum from 1-2 nm relative to the shorter wavelengths less
158 than 1 nm. As discussed by Siskind et al., (2022) this seems consistent with Orbiting Solar
159 Observatory (OSO) data presented by Neupert et al (1967), although this spectral region is not
160 well covered with modern spectra. Comparing our results in detail with Rodgers et al., suggests
161 that our 0.1 – 1 nm result ($.004 \text{ W/m}^2$) agrees well. Our 1-2 nm integrated energy is about 20%
162 lower than theirs at flare peak. For the purposes of this paper, this difference is not significant;
163 when we compare our calculated nitric oxide variation to Rodgers et al (2010), we can account
164 for this difference by using integrated energy as the independent variable to normalize both our
165 calculations. This will be discussed further in Section 4.

166

167

168

169

170

171

172

173

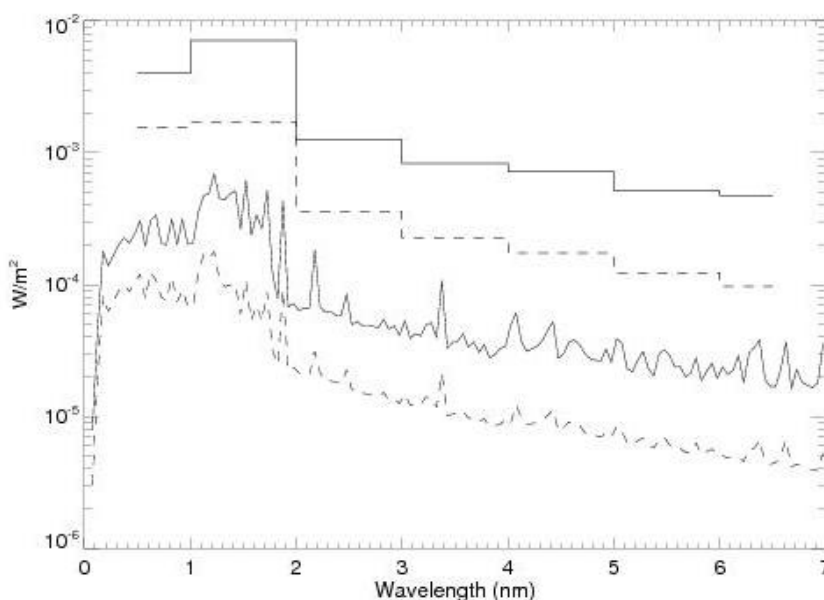
174

175

176

177

178



177

178

179 **Figure 1.** Calculated spectra for the peak of the X27 event of October 28, 2003 (solid lines) and the X13
180 event of Sept 10 2017. The rationale for the classifications is discussed in the text. The bottom two curves
181 are at 0.5 \AA resolution. The histogram format for the top two curves is the integrated energy over 1 nm
182 bins.

183

184 2.2. Atmospheric modeling with the TIME-GCM

185 The solar spectra shown in Figure 1 were used as inputs into the photoelectron ionization model
186 presented by Siskind et al (2022) and incorporated into the NCAR TIME-GCM. The NCAR
187 TIME-GCM is a hydrostatic general circulation of the middle and upper atmosphere that solves
188 the continuity, electrodynamic, energy, and momentum equations from first principles on a



189 regular longitude and latitude and log pressure grid in the vertical (Roble and Ridley, 1994). The
190 model resolution is $2.5^\circ \times 2.5^\circ$ (longitude x latitude) and 4 grid points per vertical scale height
191 extending from 12 to 4.6×10^{-6} hPa (or roughly 30 to 450-600 km depending on solar activity).

192 The photoelectron ionization model presented by Siskind et al (2022) defines 12 new wavelength
193 bins for the soft X ray energy range to give better spectral resolution (and hence better altitude
194 resolution of energy deposition) than the original NCAR spectral model presented by Solomon
195 and Qian (2005). Note, there is a typographical error in Table 3 of Siskind et al., (2022), bin #7
196 for the O₂ cross section. It should read 1.5E-20, not 1.5E-21. It is correctly implemented in the
197 model.

198 One difference in how we used the TIME-GCM from the short term (< 1 day) simulations of
199 Siskind et al (2022) concerns the dynamics of the mesosphere. In the standard version of the
200 TIME-GCM (i.e., the model setup used in Siskind et al., (2022)) climatological background
201 horizontal winds, temperatures, and geopotential are used at the model lower boundary in
202 combination with monthly mean diurnal and semidiurnal tides from the Global Scale Wave
203 Model (GSWM; Zhang et al., 2010a,b). However, this standard model configuration does not
204 properly simulate the downward transport of NO_x from the mesosphere into the stratosphere. In
205 order to do so, we constrained TIME-GCM upper stratospheric and mesospheric horizontal
206 winds and temperatures between the model lower boundary (~30 km) and ~75 km with Modern
207 Era Retrospective-analysis for Research and Applications - version 2 (MERRA-2, Gelaro et al.,
208 2017) using four dimensional tendency nudging (originally termed 4D data assimilation by
209 Stauffer and Seaman, (1990, 1994)). This nudging procedure is described in great detail by Jones
210 et al. (2018), and involves adding an additional acceleration and energy tendency term to the
211 conservation equations that is proportional to the modeled and MERRA-2 horizontal wind and
212 temperature differences up to ~75 km.

213

214 In previous studies (e.g., Jones et al., 2020; 2023), TIME-GCM was constrained using a high-
215 altitude version of the Navy Global Environmental Model (NAVEM-HA, Eckermann et al.,
216 2018; McCormack et al., 2017), which provides dynamical fields up to ~97 km. Note the
217 MERRA-2 reanalysis product used herein does not extend as high as NAVEM-HA, and
218 therefore, we had to make a small modification to equation 5 of Jones et al. (2018). This equation
219 describes the vertical weighting distribution of nudging, which in part controls the strength of the
220 additional tendency term. The vertical weighting distribution used here takes the same functional
221 form as equation (5) of Jones et al. (2018), but the z_{max} variable (representative of the TIME-
222 GCM log-pressure level where the model becomes unconstrained) is equal to -10.5 or ~75 km.
223 For reference, a vertical weighting factor of 0.5 occurs roughly at 55 km (or 0.2 hPa), above
224 (below) which the nudging term is more weighted toward TIME-GCM (MERRA-2) dynamical
225 fields.

226

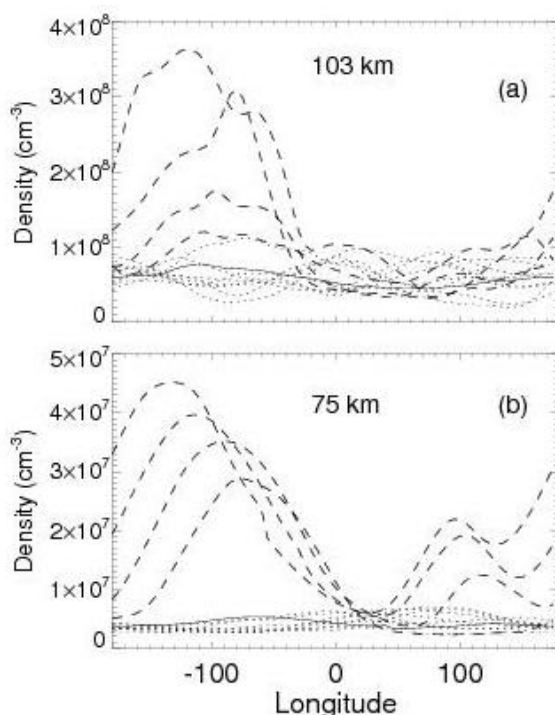
227 2.3 Initial thermospheric response to multi-month solar flare

228 As discussed above, we model the effects of supernova induced soft X ray event as if it were a
229 multi-month solar flare. Specifically, for the X13 event, we performed a simulation which
230 continues through the end of 2017 and then covers a complete additional year. In the analyses
231 discussed below, we present the results of the X13 and X27 simulations with a baseline run that



232 only includes the EPP-IE effect. The difference between the X13 or X27 and baseline runs serve
233 to quantify the possible response of the middle and upper atmosphere to a multi-month soft X-
234 ray event. We also note that for TIME-GCM simulations performed herein geomagnetic activity
235 was held constant with $K_p \cong 3$ in order to exclusively highlight flare impacts.

236 Figure 2 shows the initial response at low latitudes (averaged from 30S-30N), plotted every two
237 hours, as a function of longitude for the first day. The solid line is 1600 UT which was just at
238 flare onset (the peak of the Sept 10, 2017 flare was around 1606 UT). The four dashed lines are
239 for 1700, 1900, 2100 and 2300 UT and show how the NO increases both in the thermosphere
240 (panel (a)) and in the mesosphere (panel (b)) immediately after flare onset. Note how the
241 longitudinal response progresses westward for the equatorial plots, tracking the sub-solar point.
242 This is consistent with our implicit assumption that the supernova will be aligned with the
243 ecliptic plane. While perhaps not always true (the galactic plane is tilted 60° with respect to the
244 ecliptic plane (cf. https://en.wikipedia.org/wiki/Astronomical_coordinate_system), any
245 supernova will nonetheless rise and set like the sun, and the peak effects will, like with a solar
246 flare, be concentrated at the sub-stellar longitude. Thus we conclude that our approach of using
247 an extended solar flare event as a means of simulating a supernova soft X-ray event is
248 acceptable.



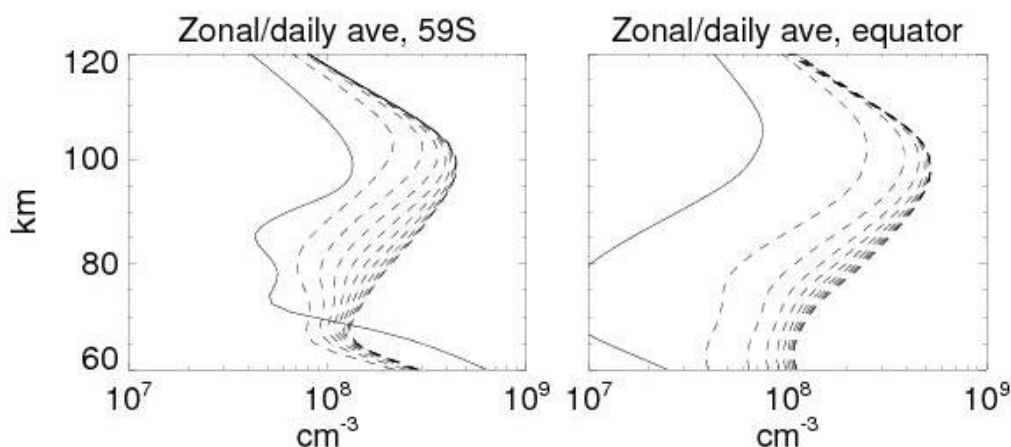
249

250 **Figure 2.** Initial response of thermospheric (panel (a)) and mesospheric (panel (b)) nitric oxide density to
251 the onset of the extended flare. The solid line in each panel is for 1600 UT, which roughly corresponds to
252 the onset of the flare. The dotted lines are for times prior to that. The dashed curves which progressively



253 increase and phase to the left according to the sub-solar point are for hours 1700, 1900, 2100 and 2300
254 UT.

255 Figure 3 shows daily averaged profiles for the first 10 days for the event, both at low and at high
256 latitudes. The effects are largest at the equator, but are still significant at 59S, and extend well
257 down into the mesosphere. Note the changes appear to level off after several days, suggesting
258 that the initial response is saturating. Indeed we find that all the thermospheric response occurs in
259 the first 10-14 days. The middle atmosphere response includes both this initial effect and then
260 later, seasonal effects as NO is transported down from the upper mesosphere/lower
261 thermosphere.



262

263 **Figure 3.** Profiles of the first 10 days of the nitric oxide profile at two latitudes. The individual days are
264 not labeled, but the day-to-day increase in NO density is monotonic with time. The solid lines are pre-
265 flare.

266

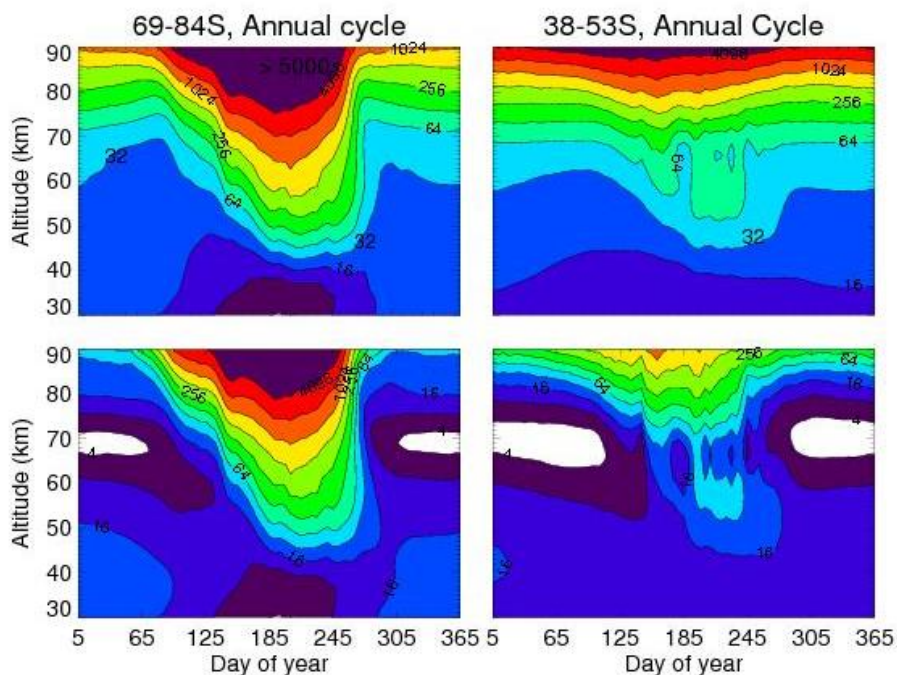
267 3. Seasonal Variation of the Xray-IE in the middle atmosphere

268 Figure 4 compares the seasonal variation of the TIME-GCM NO_x (defined as NO + NO₂) from
269 our extended flare calculation with our baseline run that only includes the EPP-IE. It thus shows
270 the seasonal variation of how the Xray-IE leads to NO_x buildup in the middle atmosphere
271 beyond that caused by energetic electron precipitation. To understand this, we first focus on our
272 baseline EPP-IE simulation and how it compares with the recent simulations of the EPP-IE from
273 Pettit et al., (2021), specifically their Figures 9-10 which they compared with Michaelson
274 Interferometer for Passive Sounding (MIPAS) data in the Southern Hemisphere. Ultimately, we
275 will conclude that the Xray-IE shows similar behavior to the EPP-IE simulation, except with a
276 larger magnitude and for a more prolonged seasonal duration. Thus to highlight the longer
277 impact, we show the entire year whereas Pettit et al. (2021) just showed April-October.

278 In comparing with Pettit's results, we see that our baseline simulation underestimates the descent
279 of the MIPAS NO_x data at the higher latitudes. The MIPAS data show the 16 ppbv contour



280 descending to below 35 km for the month of August, whereas our simulation (panel a) has this
281 contour remaining above 40 km for the late austral winter period. There are likely two reasons
282 for this. First, is likely the simple fact that TIME-GCM has a bottom boundary at 30 km and thus
283 the descent will decay as this boundary is approached. Indeed, analyses of data from both the
284 Halogen Occultation Experiment (HALOE) on board the Upper Atmospheric Research Satellite
285 (UARS) and Polar Orbiting Aerosol Measurement (POAM) data have shown that enhanced NO_x
286 can routinely be detected below 30 km in the Southern Hemisphere (Siskind et al., 2000; Randall
287 et al., 2007). Second, our model does not have the medium energy electron ionization that Pettit
288 et al (2021) discuss. They show that models without this component of energetic electrons
289 underestimate the descent into the mid-stratosphere.



290

291 **Figure 4.** Annual cycle of NO_x descent into the upper stratosphere from TIME-GCM for two latitude
292 bands. The bottom row is for a baseline simulation that only includes the EPP-IE. The top row
293 additionally includes the Xray-IE from the X13 simulation presented in Figures 1-3. The year shown is
294 2018 thus representing the period about 4-12 months after flare onset on Sept, 10, 2017. The values on the
295 contour labels are in units of ppbv. The white colored regions in the baseline run are for mixing ratios < 4
296 ppbv.

297 On the other hand, our baseline simulation does much better at mid-latitudes (38-53S in the
298 figure). It shows the 16 ppbv contour dipping down to 45 km for a couple of months. This is
299 quite similar to the MIPAS data shown by Pettit et al., (2021) and is consistent with Funke et al
300 (2005) and Arnone and Hauchecorne (2011) who pointed out that there are two components to
301 the descent of upper atmospheric NO_x into the stratosphere. One component is directly into the



302 stratospheric polar vortex and descends down into the mid-stratosphere; as we note above, our
303 model cannot capture this. However, there is a second component that is dispersed into middle
304 latitudes in the upper stratosphere. It appears that our model does capture this and it could be
305 argued that from a global biospheric perspective, this second component is more important since
306 a greater region of the globe is affected.

307 Regarding our Xray-IE simulation, dramatic effects are clearly seen in the mesosphere, both mid
308 and high latitudes. The mesospheric minima near 70 km are completely filled in and mixing
309 ratios of over 32 ppbv, up to near 100 ppbv, are seen for most of the year. However, for
310 considerations of impacts on ozone, we focus more on the stratospheric effects. Here, at first
311 glance, for the higher latitudes, the IE-Xray effect appears somewhat muted. We see no
312 difference in the maximum value of NO_x descending below 50 km between our baseline and
313 constant X13 simulation. However, the IE-Xray effect is somewhat more prolonged in its NO_x
314 enhancement. The baseline simulation shows the 16 ppbv contour curving sharply upward
315 around Day 270. Thus NO_x values near 50 km decrease abruptly and this is similar to what is
316 seen in Pettit et al.'s MIPAS data. However, the X13 simulation shows the upper stratospheric
317 NO_x values remaining between 16-32 ppbv for the entire austral spring.

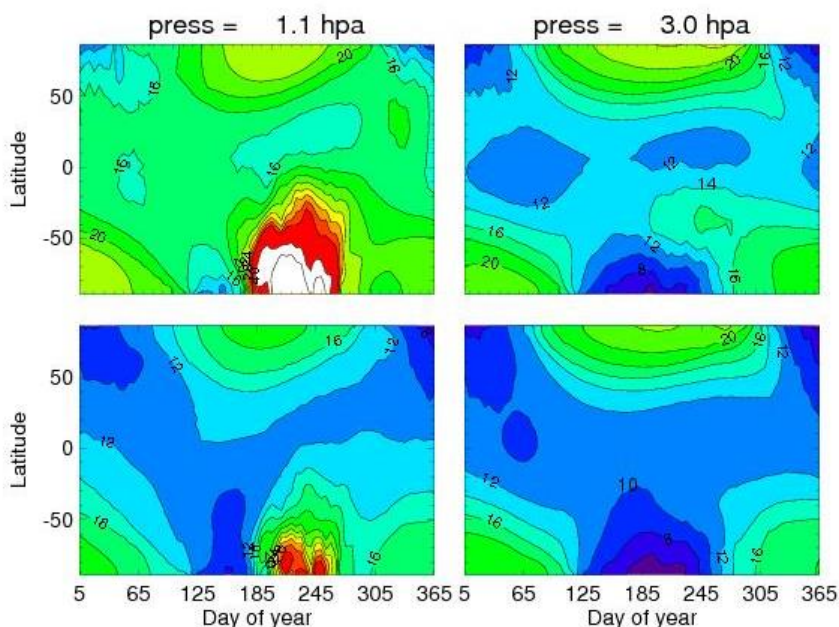
318 At mid-latitudes, the effect of the continual soft X-ray flux is more pronounced. Whereas the
319 baseline simulation shows 16 ppbv descending to about 45 km, the flare simulation has about
320 double that. Like the high latitude case, after approximately Day 270, the baseline case NO_x
321 values fall below 16 ppbv, in agreement with the MIPAS data. By contrast, in the X13
322 simulation we see NO_x values of 32-64 ppbv descending to 45-50 km and the entire upper
323 stratosphere remains flooded with enhanced NO_x values greater than 16 ppbv for the whole year.

324 Figure 5 also compares our baseline (EPP-IE only) simulation with that including the Xray-IE,
325 this time for two pressure surfaces as a function of latitude and time: one near the stratopause
326 (the indicated pressure roughly corresponds to altitudes of 45-48 km) and one lower down
327 towards the middle stratosphere (approximately 38-40 km). The figure shows how the NO_x from
328 the flare/supernova spreads over the Southern Hemisphere. It is useful to first look at our
329 baseline case; it clearly shows that the EPP-IE effect is mainly in late winter/early spring in the
330 Southern Hemisphere and covers the latitudes from -80 to about -20 or -30. Note, there is no
331 evidence for this seen at 3.0 hPa whereas in actuality, there should still be a spring time
332 enhancement in the highest latitudes as we discussed above. When we compare this with the top
333 row in the figure, the effects of the soft X-rays are very apparent. The late winter/spring
334 enhancement at 1.1 hPa is about twice as large and there is now seen an enhancement at 3.0 hPa
335 whereby values of NO_x of 10-12 ppbv at Southern mid-latitudes are now replaced by values of
336 14-16 ppbv. Importantly, there is no evidence for significant enhancements in the Northern
337 Hemisphere although there does seem to be a general global increase in NO_x of about 2 ppbv-
338 about 20% above the baseline values. This lack of significant NH enhancement is consistent with
339 observations of the EPP-IE which show generally weaker effects in the NH relative to the SH
340 (Funke et al., 2014). This is generally believed to be due to the weaker descent in the NH and the
341 greater horizontal mixing due to mesospheric planetary waves (Siskind et al., 1997), although
342 NH enhancements are seen in specific years with very strong dynamical perturbations (cf. Funke



343 et al., 2017). In the present case, while we will consider the effects on stratospheric ozone below,
344 it does suggest a limit as to how biospherically destructive the soft X-ray event could be since
345 the effects are likely to be much more muted in the NH

346



347

348 **Figure 5.** NO_x (ppbv) vs latitude and day of year. The period of time is the same as shown in Figure 4.
349 The bottom row is for the baseline case without enhanced soft X-rays; the top row includes the
350 continuous X13 flux. The red regions are NO_x values greater than 28 ppbv; the white regions are NO_x
351 values greater than 40 ppbv.

352 One final consideration in looking at the annual cycles in the upper stratosphere mesosphere in
353 Figures 4 and 5 is that there appears to be no evidence for any continual buildup of NO_x. The
354 NO_x at the end of 2018 is not much different than at the beginning. This is consistent with
355 Figure 3 in that the day-to-day NO increase in the thermosphere decreases such that after 10 days
356 the NO profile showed little change. This will be important when we try to extrapolate from our
357 X13 simulation to stronger events.

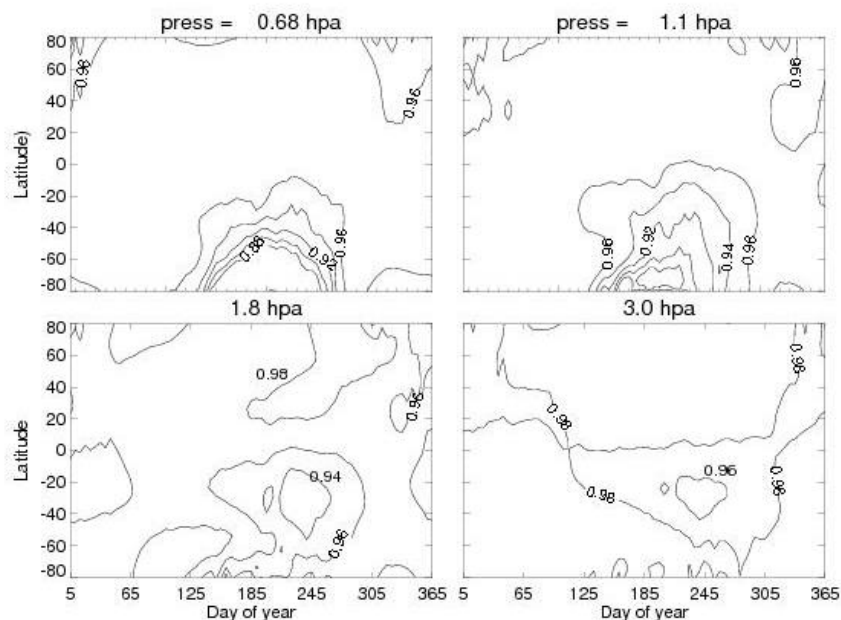
358

359 Figure 6 shows the global change in ozone for the X13 simulation compared with our baseline
360 EPP-IE only case for four pressure surfaces ranging from 0.68 to 3.0 hPa. The values are less
361 than 1.0 globally for the entire year which means lower ozone for the X13 simulation. However,
362 there is a clear maximum in the reduction for the late winter/early spring period in the SH,
363 consistent with the global distribution of the enhanced NO_x shown in Figure 5. Note that the
364 fractional reduction is larger at the lowest pressures. Normally, at these altitudes in the lower



365 mesosphere, ozone loss is dominated by the HO_x catalytic cycle (Brasseur and Solomon, 2005).
366 However, with NO_x enhancements on the order of 100 ppbv, the NO_x catalytic cycle can
367 dominate up to higher altitudes (lower pressures) than is conventional. At the same time, since
368 the bulk of the ozone density is in the stratosphere, the effect of a 3-4% reduction at 3.0 hPa is of
369 greater impact than a 10% reduction at 0.68 hPa.

370 The results show here clearly suggest a potentially global effect on the ozone, albeit limited to a
371 couple of months when the SH NO_x enhancement has spread to the equator. The effect is not
372 large- about 5% locally in the upper stratosphere and thus unlikely to be biospherically
373 significant. However, there are important caveats to this statement that we will explore in the
374 subsequent section. First, as we noted above, our input Xray energy is much smaller than the
375 supernova soft Xray events postulated by Brunton et al (2023). Second, the TIME-GCM is
376 limited by a bottom boundary at 30 km. About half of the stratospheric ozone column lies below
377 this altitude and must be considered before drawing any conclusions. We consider both these
378 issues in the sections below.



379
380 **Figure 6.** Annual variation of the ratio of ozone from the X13 simulation compared with the baseline
381 simulation at the 4 indicated pressure surfaces

382

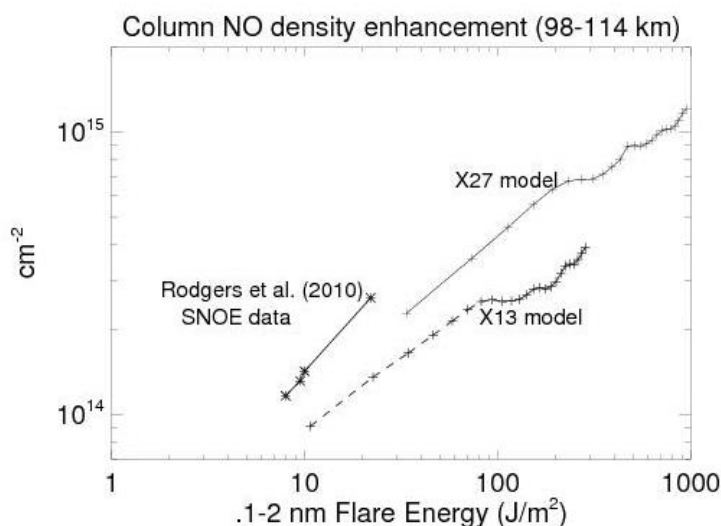
383 4. Extrapolation to higher Xray fluxes and impact on stratospheric ozone

384 To extrapolate our NO/flare response, we first seek to compare our results with observations of
385 the NO response to solar flares. The only quantitative analysis of the response of nitric oxide to a



386 solar flare that we are aware of is that by Rodgers et al. (2010) using data from the Student Nitric
387 Oxide Explorer (SNOE). SNOE was particularly well suited to study the NO response to a solar
388 flare because it was in a sun-synchronous orbit with an equator crossing time in the late morning
389 when the sun was relatively high in the sky. Rodgers et al. calculated the NO column change
390 observed by SNOE and plotted it versus the integrated soft Xray input energy derived from a
391 catalog of 11 flares.

392 Figure 7 compares the TIME-GCM results to Rodgers. The figure shows the integrated energy
393 from the four strongest X-class flares observed by SNOE with the largest being the so-called
394 Halloween event of October 28, 2003. As noted above, this event, labeled as X18 in Rodgers et
395 al.'s Table 3, is now recalibrated to be X25, and in our simulation with NRLFLARE it is a bit
396 higher at X27. Also shown are the TIME-GCM calculated hourly column NO from the local
397 equatorial sub-solar longitude for each of the first 24 hours of our model simulations for the X13
398 and X27 events.



399

400 **Figure 7.** Calculated TIME-GCM NO column density enhancement from the X13 and X27 simulations
401 compared with the observed NO increases reported by Rodgers et al. (2010) for the 4 strongest flares
402 listed in their Table 3. The plus symbols on the model curves represent output for every hour. The first
403 points shown for each of the model account for the number of minutes after each integral hour that the
404 flare peaked. Thus the X13 flare peak was at 16.1 UT (cf. Table 1 of Siskind et al., 2022) and thus the
405 first point shown for the X13 model represents 54 minutes of photon flux. Like Rodgers et al. (2010), we
406 subtracted the pre-flare NO column in the model before calculating the enhancements shown.

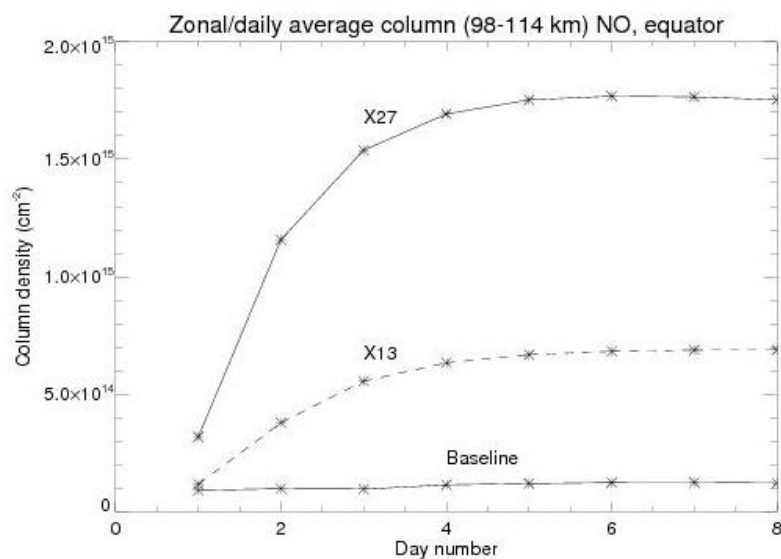
407

408 In general, the figure shows a quasi-linear relationship between column NO and the integrated
409 energy for both SNOE and the two model simulations. It appears that the rate of energy input is
410 important for the NO increase. Thus after two model hours, the X13 simulation accrues the same
411 energy input as the 27 minute long October 28, 2003 flare and yet the NO column response is



412 well below the observations. The column NO for the X13 simulation takes over 4X the energy
413 input of the observed flare to reach the same enhancement as observed by SNOE. The column
414 NO for our X27 simulation, which is designed to simulate the October 28, 2003 flare comes
415 closer and matches the SNOE data just after the first hour of the model simulation (actually 51
416 minutes since the flare peak was at 9 minutes past 11 UT and model output was only saved
417 hourly). However, since the actual October 28 flare only lasted 27 minutes, it means that the
418 TIME-GCM is calculating a smaller NO column for the same energy input than was recorded by
419 SNOE. Rodgers et al. (2010) reported an observed column enhancement of $2.6E14 \text{ cm}^{-2}$ for solar
420 X ray input of 22.4 J/m^2 where, reading from the graph, the TIME-GCM requires closer to 40
421 J/m^2 before reaching this level of NO enhancement.

422 After 24 hours, Figure 7 shows that the X27 simulation produces about a factor of 3 more NO
423 than the X13 simulation. Figure 8 shows the daily averaged, zonal mean column NO for both
424 models extended out to the full 8 days of the X27 simulation before the model crashed. Similar
425 to Figure 3, it shows that both models level out after several days. The ratio of the two column
426 densities equilibrates to a slightly smaller value than seen in Figure 7, about a factor of 2.6. The
427 fact that the column densities level out can offer a useful guide for extrapolating our middle
428 atmosphere NO_x enhancements even without completing a full year with the X27 simulation. It
429 suggests that the reasonable enhancements might lie in the range of a factor of 2-3 over the X13
430 simulation. We will explore this below.



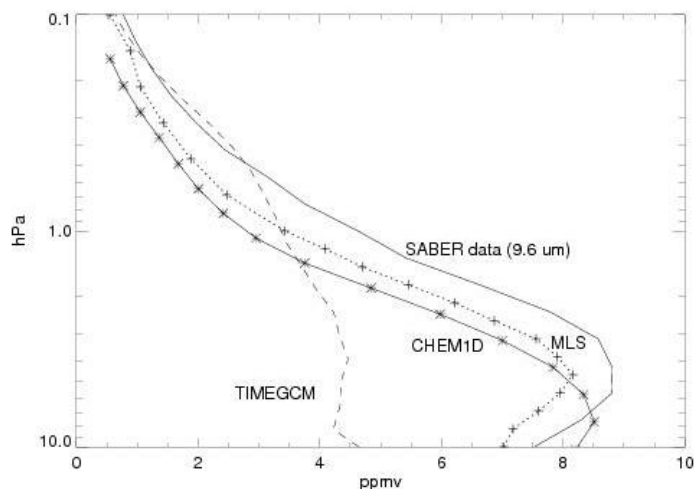
431

432 **Figure 8.** Daily and zonally averaged equatorial column densities for the X27 (solid line with stars) and
433 X13 (dashed line with stars) TIME-GCM simulations. A baseline case run for the conditions of
434 September 2017, but with no flare/supernova and which remains at approximately $1 \times 10^{14} \text{ cm}^{-2}$ is also
435 shown.



436 To evaluate in detail how ozone may be reduced for the X27 simulation, we will use the
437 CHEM1D photochemical box model. This model has previously been used to model satellite
438 observations of mesospheric OH (Siskind et al., 2013) and validate ground based measurements
439 of ClO (Nedoluha et al., 2020). It is important to first evaluate the model's ability to calculate
440 stratospheric ozone since, as is most recently discussed by Diouf et al. (2024), chemical models
441 of upper stratospheric and lower mesospheric ozone historically fall short of fully reproducing
442 observations.

443 Figure 9 shows a comparison of CHEM1D and TIME-GCM ozone with two observations from
444 September 2nd, (Day of year 245) 2018 at a latitude of 38-40S. This period and location was
445 selected because it corresponds to the time and location of the most significant upper
446 stratospheric ozone depletions indicated by the TIME-GCM in Figure 6. The observations are
447 from the 9.6 μm measurement of the Sounding of the Atmosphere with Broadband Emission
448 Radiometry (SABER) instrument on board the NASA TIMED satellite and the Microwave Limb
449 Sounder (MLS) from the NASA Aura satellite. SABER and MLS data have long been the
450 standards for measuring middle atmospheric ozone globally. Figure 9 shows, first, that TIME-
451 GCM is ill suited for model-data comparisons of stratospheric ozone. This is perhaps not a
452 surprise- the model was designed to study middle atmospheric dynamics and transport and its
453 coupling to the upper atmosphere (Roble et al., 1994). For example, TIME-GCM does not
454 include all the active chlorine and nitrogen species that are required for a comprehensive model
455 of stratospheric ozone. Thus for chlorine, TIME-GCM has Cl and ClO, but not HOCl. For
456 nitrogen, TIME-GCM only has NO and NO₂, but not HNO₃ or N₂O₅. By contrast, CHEM1D
457 does include these species. The comparison with CHEM1D very closely matches that seen by
458 Siskind et al. (2013), who used CHEM1D for mesospheric ozone and hydroxyl and Diouf et al.
459 (2024), who used the model of Bertaux et al. (2020) and compared with MLS ozone and SABER
460 O₂(¹ Δ) 1.27 μm emission. In all cases, the model falls short of completely reproducing the
461 observations. Both Siskind et al. (2013) and Diouf et al. (2024), having exhausted all possibilities
462 for reaction rate changes and possible temperature inputs, invoked the possibility of an additional
463 source of ozone from vibrationally excited oxygen as hypothesized by Slanger et al., (1988) and
464 Price et al., (1993). The purpose here is not to answer this long standing question; rather, Figure
465 9 shows that CHEM1D does as well as could be expected given our understanding of middle
466 atmospheric ozone photochemistry. Our purpose here is to perform sensitivity studies for varying
467 amounts of NO_x, guided by our TIME-GCM simulations. Figure 9 shows that CHEM1D is
468 adequate for this task. We should additionally note that as one moves towards higher pressures
469 greater than 5 hPa, the chemical lifetime of ozone becomes longer such that it is no longer under
470 pure chemical control but also dynamical influences. Thus, the apparent improved agreement
471 with the observations near 10 hPa should not be over-interpreted.



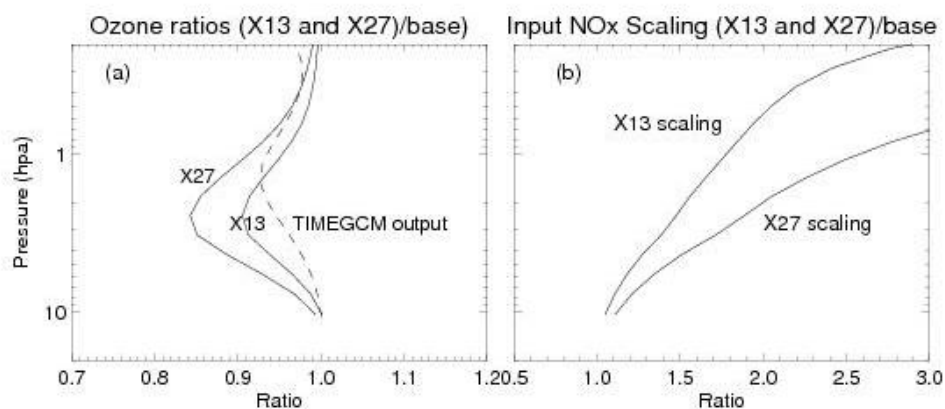
472

473 **Figure 9.** Comparison of the TIME-GCM (long dashes) and CHEM1D (solid line with stars) models with
474 SABER (solid line) and MLS (dotted line with plus symbols) observations of ozone. The location is 38-
475 40S and the time of year is September 2nd, 2018. CHEM1D used temperature and pressure and NO_x
476 abundances from the TIME-GCM as input. The approximate altitude range corresponding to the y-axis is
477 about 30-62 km.

478 We now show the fractional ozone depletions, as a function of pressure, from the enhanced NO_x
479 due to a multi-month solar flare. Figure 10 presents the calculated ozone loss ratios (panel a) for
480 two models of CHEM1D that use enhanced NO_x compared with the baseline simulation
481 presented in Figure 9. The location and time of year is the same as in Figure 9. The NO_x
482 enhancements (panel b) are taken from the X13 simulation shown in the previous figures plus an
483 extrapolated enhancement (the greater of the curves in Figure 10) based upon the short term
484 response shown in Figure 8. Figure 10 also shows the vertical profile of the TIME-GCM ozone
485 change taken from Figure 6.



486



487

488 **Figure 10.** (a) Ratios of calculated ozone from CHEM1D compared with a baseline (no flare) case for
489 September 2, at a latitude of 39S. The two solid lines use NO_x input according to the scaling ratios
490 shown in panel (b) The X13 scaling is based upon the NO_x shown in Figures 3-5. The X27 scaling is a
491 hypothesized extrapolation based upon Figure 8 and discussed in the text. Also shown as the dashed line
492 in panel (a) is the ozone ratio from the TIME-GCM as per the surface contour plots shown in Figure 6.

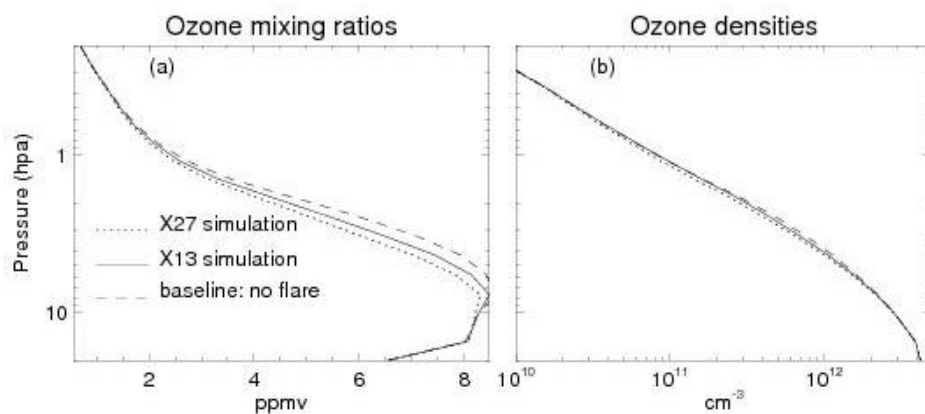
493

494 Figure 10 shows that for the X13 case, we could expect ozone depletions of up to 8% in the
495 upper stratosphere. For the more significant X27 case (i.e. for a more intense supernova X-ray
496 event), we might see ozone reductions of up to 15-18% in the upper stratosphere. Figure 10 also
497 shows the vertical profile of the TIME-GCM ozone reduction. It does not exactly match the
498 profiles from CHEM1D in terms of shape and altitude of peak reduction, but it is very close to
499 the X13 CHEM1D simulation in terms of giving a peak loss of 6-7% in the upper stratosphere.
500 The TIME-GCM result is useful because it allows our detailed CHEM1D calculations to be
501 placed in the global context shown in Figure 6.

502 Based upon Figure 10 and Figure 6, we can conclude that a supernova X-ray event could cause
503 widespread ozone loss in the 10-20% range in the upper stratosphere for late winter/early spring
504 in the Southern Hemisphere. While this would likely be easily observable with suitable
505 instrumentation, it is less likely to have a dramatic biospheric effect. This is because most of the
506 stratospheric ozone is found at altitudes from 20-35 km (5 hPa-50 hPa pressure levels). The
507 losses shown in Figure 10 are only the upper edge of that layer. This is shown in Figure 11,
508 which shows the actual ozone mixing ratios (panel (a)) and ozone density profiles (panel (b))
509 which correspond to the scaling ratios shown in Figure 10. In the case where the model output is
510 shown as ozone densities, the curves are almost indistinguishable. The change in the total
511 column ozone, which is most relevant for surface UV exposure, is 1% for the X13 simulation
512 and 2% for the X27 extrapolation.



513



514

515 **Figure 11.** Absolute ozone abundances corresponding to the ratios presented in Figure 10. The three
516 simulations are labeled in panel (a). They are identically shown in density units in Panel (b) but are
517 almost indistinguishable because the 8-15% reductions are very hard to see on a graph that covers over
518 two orders of magnitude.

519

520 5. Discussion and conclusions

521 Our results clearly suggest the strong possibility of globally widespread ozone loss in the upper
522 stratosphere, at least for a period of a couple of months in the Southern Hemisphere. However, at
523 the same time, we conclude that this is unlikely to have a global biospheric impact because the
524 depletion is limited to the upper edges of the ozone layer. This limitation is derived from our
525 simulations showing that, like the EPP-IE, the Xray-IE does not penetrate below 35-40 km on a
526 global basis. At polar latitudes, our results allow us to speculate that a supernova could greatly
527 exacerbate the ozone hole. Or even, for atmospheres without anthropogenic chlorine, create an
528 ozone hole. Indeed, it has already been noted that the EPP-IE has been confused with an
529 expansion of the ozone hole due to volcanic aerosols (cf. Siskind et al., 2000 and discussion
530 therein). However, since the hole is generally confined to the polar vortex, the effects of the
531 Antarctic ozone hole have not caused widespread global ecological destruction although regional
532 effects may be occurring (Robinson et al., 2024). There are likely other more subtle hypothesized
533 effects of the enhanced NO_x that we do not address. For example, we do see moderate NO_x
534 enhancements throughout the Northern Hemisphere and it has been suggested that EPP-IE in the
535 Northern Hemisphere has effects on stratospheric and possibly tropospheric meteorology
536 (Seppala et al., 2009). Our work here cannot rule this out for the Xray-IE.

537 Certainly, our results come with large uncertainties that would be useful to address. Perhaps the
538 biggest is that the TIME-GCM, with a bottom boundary above the peak of the ozone layer, is not
539 designed to study stratospheric chemistry. Moreover, the 30 km bottom boundary prevents us
540 from studying descent of NO_x enriched air down to the lower altitudes where the EPP-IE has



541 been observed in the SH polar vortex (Randall et al., 2007). Thus our comments about the ozone
542 hole are necessarily speculative. In addition, our simulation of the NO produced during solar
543 flares appears to be less than observed by SNOE. This might mean that the NO response to a
544 flare would be greater than we suggest, perhaps by as much as a factor of 2. Here it would be
545 very helpful if there were another dataset that could corroborate the NO response reported by
546 Rodgers et al., (2010). As we noted above, the local time of the sun-synchronous SNOE orbit
547 was ideal for observing solar flares. By contrast, more recent NO observations which are
548 summarized in Table 1 and Figure 3 of Emmert et al., (2022) are less well suited. Emmert et al.
549 (2022) show that, for example, the Atmospheric Chemistry Experiment (ACE) and the Solar
550 Occultation for Ice Experiment (SOFIE) on the NASA/AIM satellite used the technique of solar
551 occultation which by definition means sunrise or sunset. This type of observation is not well
552 suited to observing the effect from a flare which would be less noticeable at local sunset or
553 sunrise. Likewise the ODIN satellite which measured NO with the Sub-millimeter radiometer
554 (SMR) was in a dawn-dusk synchronous orbit. Based upon Emmert et al., (2022) it appears that
555 only MIPAS on the ENVISAT satellite was in a proper daytime orbit to see flares. An
556 examination of the MIPAS data might be an interesting test of some of our SNOE-based results.

557 Ultimately, however, even if we did underestimate the NO production by a factor of 2 or even 3,
558 the effects on the ozone column are likely not catastrophic because they will be limited to above
559 35-40 km. We point to the simulations of Thomas et al., (2007) of a possible solar proton event
560 that may have accompanied the 1859 Carrington flare event. Solar protons penetrate much
561 deeper into the stratosphere than soft X rays and thus the effect on NO_x is more direct rather than
562 indirect as simulated here. Indeed, they obtained much larger NO_x increases down to 30 km and
563 localized ozone losses near 35-40 km of greater than 30%. Despite this greater increase in NO_x
564 and greater ozone loss, their calculated perturbation to the ozone column was less than 15%
565 because the bulk of the ozone density between 20-30 km remained unaffected from the proton
566 flux. By contrast, other phenomena linked to supernovae, such as cosmic rays, are known to be
567 absorbed by the atmosphere near the peak of the ozone layer in the 20-30 km altitude range
568 (Melott et al., 2017) and, in our assessment, those are likelier candidates for causing global
569 ozone destruction that would greatly enhance the flux of destructive UV radiation to the surface.
570 However, we should conclude by noting that the destructiveness of both the gamma ray and
571 cosmic ray mechanisms have also been recently called into question (Christoudias et al., 2024).
572 Our calculations here are therefore consistent with Christoudias et al, (2024) in showing how the
573 earth's atmosphere can shield its biosphere.

574

575 *Code and Data Availability.* The TIME-GCM code is available by contacting the National Center for
576 Atmospheric Research. The model output produced herein is reproducible from the TIME-GCM model
577 source code following the discussions and implementations of the nudging schemes and lower boundary
578 conditions described thoroughly in Sections 2.4 and in Jones Jr. et al. (2018) and Jones Jr. et al. (2020).
579 Daily NCAR TGCMs outputs in netCDF format from this study are archived on the DoD HPCMP long-
580 term storage system. MERRA-2 middle atmospheric horizontal winds and temperatures used for
581 constraining TIME-GCM dynamics are available at <https://disc.gsfc.nasa.gov/datasets?project=MERRA-2>.
582 The SABER and MLS data used in Figure 9 were respectively obtained from [19](https://saber.gats-</p></div><div data-bbox=)



583 inc.com/ and <https://mls.jpl.nasa.gov/eos-aura-mls/data.php>. Other model output such as CHEM1D and
584 specific supernova output from TIMEGCM are now in the process of getting approval at NRL for
585 eventual public release and will be made available once this paper is accepted for publication.

586 *Author Contributions.* DES conceived the study, performed the analysis of the TIMEGCM
587 output, conducted the CHEM1D analysis and led the writing. MJJr. configured the TIMEGCM, both to be
588 nudged by MERRA and to input the NRLFLARE spectra, performed the simulations and wrote Section
589 2.2. JWR is the developer of NRLFLARE; he provided the soft X-ray spectra used by the TIMEGCM and
590 wrote Section 2.1.

591
592 *Competing Interests* The contact author has declared that none of the authors has any competing interests.
593

594 *Acknowledgements.* This work was supported by the Office of Naval Research. We also acknowledge the
595 NASA Living with a Star program for supporting development of NRLFLARE and the development of
596 the supernovae soft X-ray spectra. Computational resources for this work were provided by the U.S.
597 Department of Defense (DoD) High Performance Computing Modernization Program (HPCMP).
598

599 *Financial support.* This research has been supported by the Office of Naval Research (6.1
600 funding).
601

602 **References**

- 603
604 Airapetian, V. S., Barnes, Cohen et al., Impact of space weather on climate and habitability of
605 terrestrial-type exoplanets (2020), *Int'l Journal of Astrobiology*,
606 <https://doi.org/10.1017/S1473550419000132>
607
608 Arnone E. and Hauchecorne A., (2011) Stratospheric NO_y species measured by MIPAS and
609 GOMOS Onboard ENVISAT 2002-2010: Influence of plasma processes onto the observed
610 distribution and variability, *Space Sci Rev.*, 168, 315-332, DOI 10.1007/s11214-011-
611 9861-1
612
613 Bertaux, J. L., Hauchecorne, A., Lefevre, F., Breon, F. M., Blanot, L., Jouget, D., et al. (2020).
614 The use of the 1.27 μm O₂ absorption band for greenhouse gas monitoring from space and
615 application to MicroCarb. *Atmospheric Measurement Techniques*, 13(6), 3329–3374. <https://doi.org/10.5194/amt-13-3329-2020>
616
617
618 Bradshaw, S. J. and Cargill, P. J., “The Influence of Numerical Resolution on Coronal Density in
619 Hydrodynamic Models of Impulsive Heating”, *The Astrophysical Journal*, vol. 770, no. 1, IOP,
620 2013. doi:10.1088/0004-637X/770/1/12.
621
622 Brasseur G. and S. Solomon, 2005, *Aeronomy of the Middle Atmosphere*, D. Reidel Publishing
623 Co.
624
625 Brunton, I. R., O’Mahoney, C., Fields, B. D., Melott, A. L., and Thomas, B. C., (2023) X-Ray-
626 luminous Supernovae: Threats to terrestrial biospheres, *Astrophys. J.*, 947:42,
627 <https://doi.org/10.3847/1538-4357/acc728>
628



- 629 Cliver, E. W., Schrijver, C. J., Shibata, K., and Usoskin, I. G., “Extreme solar events”, Living
630 Reviews in Solar Physics, vol. 19, no. 1, 2022. doi:10.1007/s41116-022-00033-8.
631
- 632 Christoudias, T., Kirkby, J., Stolzenburg, D., Pozzer, A., Sommer, E., Brassuer, G. P., Kulmala,
633 M., Lelieveld, J., (2024) Earth’s atmosphere protects the biosphere from nearby supernovae,
634 Nature Communications: Earth and Environment, <https://doi.org/10.1038/s43247-024-01490-9>
635
- 636 Diouf M. M. N., Lefevre, F., Hauchecorne, A., and Bertaux, J.L., (2024) Three-Dimensional
637 Modeling of the O₂(¹Δ) Dayglow: Dependence on Ozone and Temperatures, *J. Geophys. Res.*,
638 <https://doi.org/10.1029/2023JD040159>
639
- 640 Eckermann, S. D., Ma, J., Hoppel, K.W., Kuhl, D. D., Allen, D. R., Doyle, J. A., et al. (2018).
641 High-altitude (0–100 km) global atmospheric reanalysis system: Description and application to
642 the 2014 austral winter of the deep propagating gravity wave experiment (DEEPWAVE).
643 Monthly Weather Review, 146(8), 2639–2666. <https://doi.org/10.1175/MWR-D-17-0386.1>
644
- 645 Emmert, J. T., Jones, M. Jr., Siskind D. E., Drob D. P., Picone, J. M., Stevens M. H., Bailey S.
646 M., Bender, S., Bernath, P. F., Funke, B., Hervig, M. E., and Perot, K. (2022) NRLMSIS 2.1: An
647 empirical model of NO incorporated into MSIS, *J. Geophys. Res.*, 127, e2022JA030896.
648 <https://doi.org/10.1029/2022JA030896>
649
- 650 Fletcher, L., et al. “An Observational Overview of Solar Flares”, Space Science Reviews, vol.
651 159, no. 1–4, pp. 19–106, 2011. doi:10.1007/s11214-010-9701-8.
652
- 653 Funke, B., Lopez-Puertas, M., Gil-Lopez, S., von Clarmann, T., Stiller, G. P., Fischer, H.,
654 Kellman, S., (2005) Downward transport of upper atmospheric NO_x into the polar stratosphere
655 and lower mesosphere during the Antarctic 2003 and Arctic 2002/2003 winters, *J. Geophys Res.*
656 ,D240308, 0148-0227/05/2005JD006463
657
- 658 Funke, B., Lopez-Puertas M., Stiller, G. P. and von Clarmann, T., (2014) Mesospheric and
659 stratospheric NO_y produced by energetic particle precipitation during 2002–2012, *J. Geophys.*
660 *Res*, 119, 4429, 10.1002/2013JD021404
661
- 662 Funke B., Ball, W., Bender, S., Gardini, A., Harvey, V. L., Lambert, A., et al. (2017) HEPPA-II
663 model–measurement intercomparison project: EPP indirect effects during the dynamically
664 perturbed NH winter 2008–2009, *Atmos. Chem. Phys*, 17, 3573-3604, doi:10.5194/acp-17-3573-
665 2017.
666
- 667 Garcia, H. A., “Temperature and Emission Measure from Goes Soft X-Ray Measurements”,
668 Solar Physics, vol. 154, no. 2, pp. 275–308, 1994. doi:10.1007/BF00681100.
669
- 670 Garcia-Sage, K, Farrish A.O, Airapetian, V. S., (2023), Star-exoplanet interactions, A growing
671 interdisciplinary field in heliophysics, *Frontiers in Astronomy and Space Science*, vol. 10, doi:
672 10.3389/fspas.2023.1064076
673



- 674 Gehrels, N., Laird, C. M. Jackman, C. H., Cannizzo, J. K., Mattson, B., J., and Chen, W., (2003)
675 Ozone depletion from nearby supernovae, *The Astrophysical Journal*, 585:1169-1176.
676
- 677 Gelaro, R. et al. (2017), The modern-era retrospective analysis for research and applications,
678 version 2 (MERRA-2), *J. Clim.*, 30(14), 5419–5454, doi:10.1175/JCLI-D-16-0758.1.
679
- 680 Jones, M., D. P. Drob, D. E. Siskind, J. P. McCormack, A. Maute, S. E. McDonald, and K. F.
681 Dymond (2018), Evaluating Different Techniques for Constraining Lower Atmospheric
682 Variability in an Upper Atmosphere General Circulation Model: A Case Study During the
683 2010 Sudden Stratospheric Warming, *J. Adv. Model. Earth Syst.*, 10(12), 3076–3102,
684 doi:10.1029/2018MS001440.
685
- 686 Jones, M. Jr., Goncharenko, L. P., McDonald, S. E., Zawdie, K. A., Tate, J., Gasperini, F., et al.
687 (2023). Understanding nighttime ionospheric depletions associated with sudden stratospheric
688 warmings in the American sector. *Journal of Geophysical Research: Space Physics*, 128,
689 e2022JA031236. <https://doi.org/10.1029/2022JA031236>.
690
- 691 Jones, M. Jr., Siskind, D. E., Drob, D. P., McCormack, J. P., Emmert, J. T., Dhadly, M. S., et al.
692 (2020). Coupling from the middle atmosphere to the exobase: Dynamical disturbance effects on
693 light chemical species. *Journal of Geophysical Research: Space Physics*, 125, e2020JA028331.
694 <https://doi.org/10.1029/2020JA028331>
695
- 696 Kahler, S. W and Ling, A. G, (2023) Solar Stellar Connection: X-ray flares to energetic (> 10
697 MeV) particle events, *Astrophys. J.*, 956, <https://doi.org/10.3847/1538-4357/acf1ff>
698
- 699 McCormack, J., Hoppel, K., Kuhl, D., deWit, R., Stober, G., Espy, P., et al. (2017). Comparison
700 of mesospheric winds from a high-altitude meteorological analysis system and meteor radar
701 observations during the boreal winters of 2009–2010 and 2012–2013. *Journal of Atmospheric
702 and Solar-Terrestrial Physics*, 154, 132–166. <https://doi.org/10.1016/j.jastp.2016.12.007>
703
- 704 Melott, A. L., Thomas, B. C., Kahcelriess, M., Semikoz, D. V., and Overholt A. C., (2017) A
705 supernova at 50 pc: Effects on the Earth’s atmosphere and biota, *Astrophys. J.*, 840,
706 <https://doi.org/10.3847/1538-4357/aa6c57>
707
- 708 Nedoluha G. N., Gomez, R. N, Boyd, I., Neal H., Parrish A., Connor B., Mooney T., Siskind, D.
709 E., Sagawa, H., and Santee, M., (2020) Initial Results and Diurnal Variations Measured by a
710 New Microwave Stratospheric CIO Instrument at Mauna Kea, *Journal Geophysical Research.*,
711 125, <https://doi.org/10.1029/2020JD033097>
712
- 713 Neupert, W. M., Gates, W., Swartz, M., & Young, R. (1967). Observation of the solar flare X-
714 ray emission line spectrum of iron from 1.3 to 20 Å. *The Astrophysical Journal*, 149, L79–L83.
715 <https://doi.org/10.1086/180061>
716
- 717 Pettit, J. M., Randall, C. E., Peck, E. D., Harvey, V. L., (2021) A new MEPED-based
718 precipitating electron data set, *J. Geophys. Res.*, <https://doi.org/10.1029/2021JA029666>
719



- 720 Price, J. M., Mack, J. A., Rogaski, C. A. and Wodtke, A. M. (1993) Vibrational-state-specific
721 self-relaxation rate constant. Measurements of highly vibrationally excited O₂ ($v=19-28$),
722 *Chemical Physics.*, 175(1),83-98, [https://doi.org/10.1016/0301-0104\(93\)80230-7](https://doi.org/10.1016/0301-0104(93)80230-7).
723
- 724 Qian L., Wang, W., Burns, A. G., Chamberlin, P. Coster, A., Zhang S-R., Solomon, S., (2019)
725 Solar Flare and Geomagnetic Storm Effects on the Thermosphere and Ionosphere During 6–11
726 September 2017, *J. Geophys. Res.*, 124, 1298, <https://doi.org/10.1029/2018JA026175>
727
- 728 Randall, C. E., Harvey, V. L., Singleton, C. S. et al., (2006) Enhanced NO_x in 2006 linked to
729 strong upper stratospheric Arctic vortex, *Geophys. Res. Lett.*, 33, L18811,
730 doi:10.1029/2006GL027160.
731
- 732 Randall, C. E., Harvey, V. L., Singleton, C. S. et al., (2007) Energetic particle precipitation
733 effects on the Southern Hemisphere stratosphere in 1992-2005 *J. Geophys. Res.*, 112., D08308,
734 doi:10.1029/2006JD007696,
735
- 736 Redmon, R. J., Seaton, D. B., Steenburgh, J. R., He, J., & Rodriguez, J. V. (2018). September
737 2017's geoeffective space weather and impacts on Caribbean radio communications during
738 hurricane response. *Space Weather*, 16(9), 1190–1201. <https://doi.org/10.1029/2018SW001897>
- 739 Reep, J. W., and Airapetian, V., (2023) Understanding the duration of solar and stellar flares at
740 various wavelengths, *Astrophys. J.*, vol. 98, DOI 10.3847/1538-4357/acf45a
- 741 Reep, J. W., Bradshaw, S. J., Crump, N. A., and Warren, H. P., “Efficient Calculation of Non-
742 local Thermodynamic Equilibrium Effects in Multithreaded Hydrodynamic Simulations of Solar
743 Flares”, *The Astrophysical Journal*, vol. 871, no. 1, IOP, 2019. doi:10.3847/1538-4357/aaf580.
- 744 Reep, J. W., Siskind, D. E., and Warren, H. P., “Solar Flare Irradiance: Observations and
745 Physical Modeling”, *The Astrophysical Journal*, vol. 927, no. 1, IOP, 2022. doi:10.3847/1538-
746 4357/ac4784.
- 747 Reep, J. W., Warren, H. P., Moore, C. S., Suarez, C., and Hayes, L. A., “Simulating Solar Flare
748 Irradiance with Multithreaded Models of Flare Arcades”, *The Astrophysical Journal*, vol. 895,
749 no. 1, IOP, 2020. doi:10.3847/1538-4357/ab89a0.
750
- 751 Robinson, S. A, Revell, L. E., Mackenzie, R., Ossala, (2024) Extended ozone depletion and
752 reduced snow and ice cover- Consequences for Antarctic biota, *Global Change Biology*,
753 <https://doi.org/10.1111/gcb.17283>
754
- 755 Roble, R. G., and Ridley, E. C. (1994) A thermosphere-ionosphere-mesosphere-electrodynamics-
756 General Circulation Model (TIME-GCM): Equinox solar cycle minimum simulations (30-500
757 km), *Geophys. Res. Lett.* 417-420.
758
- 759 Rodgers, E. M., Bailey, S. M., Warren, H. P., Woods, T. N., and Eparvier, F. G., (2010), Nitric
760 oxide density enhancements due to solar flares, *Adv. Sp. Res.*, 45,28-38.
761



- 762 Seppala, A., Randall, C. E., Clilverd, M. A., Rozanov, E., and Rodger, C. J., (2009)
763 Geomagnetic activity and polar surface air temperature variability, *J. Geophys. Res.*, 114,
764 <https://doi.org/10.1029/2008JA014029>
765
- 766 Siskind, D. E., Bacmeister, J. T., Summers M. E., and Russell J.M. III, (1997) Two-dimensional
767 model calculations of nitric oxide transport in the middle atmosphere and comparison with
768 Halogen Occultation Experiment data, *Journal of Geophysical Research*, 102/D3, 3527-3545.f
769
- 770 Siskind, D. E., Nedoluha, G. N, Randall, C. E., Fromm, M. and Russell, J. M. III (2000) An
771 assessment of Southern Hemisphere stratospheric NO_x enhancements due to transport from the
772 upper atmosphere, *Geophys. Res. Lett.*, 329-332.
773
- 774 Siskind, D. E., Stevens, M. H., Englert, C. R. and Mlynczak M. G., (2013) Comparison of a
775 photochemical model with observations of mesospheric hydroxyl and ozone, *J. Geophys. Res.*,
776 118, 195–207, doi:10.1029/2012JD017971
777
- 778 Siskind, D. E., Jones, M., Jr., Reep., J. W., Drob, D. P. Samaddar, S., Bailey, S. M., Zhang, S-R.,
779 (2022) Tests of a new solar flare model against D and E region ionospheric data., *Sp. Wea.*, 2,
780 e2021SW003012, <https://doi.org/10.1029/2021SW003012>.
781
- 782 Slanger, T. G., L.E. Jusinski, G. Black and G. E. Gadd (1988), Vibrationally excited O₂, *Science*,
783 241, 945.
784
- 785 Solomon, S. C., and Qian L., (2005) Solar extreme-ultraviolet irradiance for general circulation
786 models, *Journal of Geophysical Research*, 110, A10306, <https://doi.org/10.1029/2005JA011160>.
787
- 788 Solomon S., Roble, R. G., and Crutzen, P. J., (1982) Photochemical Coupling Between the
789 Thermosphere and the Lower Atmosphere, 1. Odd nitrogen from 50 to 120 km, *J. Geophys. Res.*,
790 87, C9, 7206-7220.
791
- 792 Stauffer, D. R., & Seaman, N. L. (1990). Use of four-dimensional data assimilation in a limited-
793 area mesoscale model. Part I: Experiments with synoptic-scale data. *Monthly Weather Review*,
794 118(6), 1250–1277. [https://doi.org/10.1175/1520-0493\(1990\)118<1250:UOFDDA>2.0.CO;2](https://doi.org/10.1175/1520-0493(1990)118<1250:UOFDDA>2.0.CO;2)
795
- 796 Stauffer, D. R., & Seaman, N. L. (1994). Multiscale four-dimensional data assimilation. *Journal*
797 *of Applied Meteorology*, 33(3), 416–434.
798 [https://doi.org/10.1175/15200450\(1994\)033<0416:MFDDA>2.0.CO;2](https://doi.org/10.1175/15200450(1994)033<0416:MFDDA>2.0.CO;2)
799
- 800 Thomas B.C., Jackman, C. H., Melott, A.L. (2007) Modeling atmospheric effects of the
801 September 1859 solar flare, *Geophys. Res. Lett.*, 34, L06810, doi:10.1029/2006GL029174.
802
- 803 Vink, J., “Supernova remnants: the X-ray perspective”, *Astronomy and Astrophysics Review*, vol. 20,
804 Springer, 2012. doi:10.1007/s00159-011-0049-1.
805
- 806 Zhang, X., Forbes, J. M., & Hagan, M. E. (2010a). Longitudinal variation of tides in the MLT
807 region: 1. Tides driven by tropospheric net radiative heating. *Journal of Geophysical Research*,
808 115, A06316. <https://doi.org/10.1029/2009JA014897>



809
810 Zhang, X., Forbes, J. M., & Hagan, M. E. (2010b). Longitudinal variation of tides in the MLT
811 region: 2. Relative effects of solar radiative and latent heating. *Journal of Geophysical Research*,
812 115, A06317. <https://doi.org/10.1029/2009JA014898>
813
814